Modeling multi-sensory feedback control of zebrafish in a flow

Daniel A. Burbano-L.[1], Maurizio Porfiri[1,2*]

1 Department of Mechanical and Aerospace Engineering, New York University, Tandon School of Engineering, 6 MetroTech Center, Brooklyn, NY 11201, USA
2 Department of Biomedical Engineering, New York University, Tandon School of Engineering, 6 MetroTech Center, Brooklyn, NY 11201, USA

* mporfiri@nyu.edu

Abstract

Understanding how animals navigate complex environments is a fundamental challenge in biology and a source of inspiration for the design of autonomous systems in engineering. Animal orientation and navigation is a complex process that integrates multiple senses, whose function and contribution are yet to be fully clarified. Here, we propose a data-driven mathematical model of adult zebrafish engaging in counter-flow swimming, an innate behavior known as rheotaxis. Zebrafish locomotion in a two-dimensional fluid flow is described within the finite-dipole model, which consists of a pair of vortices separated by a constant distance. The strength of these vortices is adjusted in real time by the fish to afford orientation and navigation control, as a function of the multi-sensory input from vision, lateral line, and touch. Model parameters for the resulting stochastic differential equations are calibrated through a series of experiments, in which zebrafish swam in a water channel under different illumination conditions. The accuracy of the model is validated through the study of a series of measures of rheotactic behavior, contrasting results of real and *in-silico* experiments. Our results point at a critical role of hydromechanical feedback during rheotaxis, in the form of a gradient following strategy.

Author summary

The astounding feats of animal orientation and navigation have fascinated scientists and engineers for decades. The refined and elegant processes of orientation and navigation are generally thought to be the outcome of a complex feedback process, which involves the integration of multiple cues gathered from the surroundings. Fish rheotaxis is an innate behavior through which an animal is able to orient itself and swim against a flow current, even in the absence of visual cues. To date, little is known about the information pathways that underlay this behavior and how they are integrated. To help address this challenge, we propose a data-driven mathematical model of rheotaxis in zebrafish— an emerging species of choice in biomedical research. Our model explains how zebrafish make use of visual, hydrodynamic, and tactile cues in a feedback loop to adjust their heading and speed during swimming. We validate the accuracy of our model by comparing real and synthetic data across two experimental conditions, in which we vary the illumination of a water channel. Our results demonstrate how a simple, yet effective, feedback control mechanism can explain a complex process such as rheotaxis.

Introduction

The ability of animals to orient themselves and navigate in complex environments has fascinated scientists and engineers for decades [1–3]. Understanding the mechanism underlying this behavior is of paramount importance in behavioral ecology for elucidating complex processes such as foraging [4], mating [5], and survival [6]. Animal orientation and navigation has also inspired technological solutions ranging from sensors [7] to computer algorithms for coordinating teams of construction robots [8].

Animal orientation and navigation typically involves the integration of different sensory systems such as vision, olfaction, and touch. These systems are used to gather information from the surrounding environment, which are, in turn, used to "close the loop" by the animal. Using this information, the animal can adjust its position and orientation. Remarkable examples include homing in salmon, which use a combination of geomagnetic and olfactory cues to swim back to their natural streams to spawn, after spending several years in the open ocean [9, 10]. Moths, on the other hand, are able to use intermittent olfactory cues in odour plumes to control their maneuvers to reach their mating partner [11]. Interestingly, navigation and orientation can be very complex even for insects, which are far in the evolutionary tree from vertebrates [12].

In some cases, animals display a specific orientation of locomotory behavior (taxis), elicited by environmental stimuli like gravity (geotaxis) [13], light (phototaxis) [14], or fluid flow (rheotaxis). For instance, fish rheotaxis is an innate behavior from early stages of life [15] that is essential for survival [16–18]. This behavior can be performed even in the absence of visual cues [19], whereby fish can use their lateral line to aid their navigation in the dark [17, 20]. The lateral line consists of a collection of neuromasts (clusters of sensory cells), sensitive to changes of water pressure, that enable a fish to create a hydrodynamic image of the surroundings [21–23]. Empirical evidence suggests that the lateral line plays a key role in the animals' orientation process [15, 20, 24]. For example, it has been recently shown that larval zebrafish use the lateral line to estimate the local vorticity of the surrounding fluid flow, which aids their orientation process [25].

In general, rheotaxis is regarded as a multi-sensory feedback process that integrates visual, hydromechanical, olfactory, and even tactile cues [26, 27]. A full understanding of how all the sensory information is processed by rheotacting fish is yet to be established. Here, we seek to contribute insight into the mechanisms underlying rheotaxis through the development of a data-driven mathematical model of adult zebrafish locomotion in a fluid flow.

Zebrafish is a freshwater species widely used as a model organism for its several advantages, ranging from its fully sequenced genome to physiological and neurological homologies with humans [28, 29]. Zebrafish has been used in a wide array of preclinical efforts, from drug discovery [30] to the study of complex brain disorders such as depression, autism, and psychoses [31]. The possibility of investigating the neural and genetic basis of behavior through zebrafish [32] offers compelling motivation for the study of their rheotactic response.

Mathematical models of zebrafish locomotion have been shown to be a powerful tool to complement and inform experimental research. For instance, in [33], a simple mathematical model of the burst-and-coast swimming style of zebrafish, revealed that adult fish have longer coasting due to their larger body mass and higher speed at the beginning of a burst. Data-driven models of fish locomotion typically describe the time evolution of the heading and the linear speed of fish using stochastic differential equations (SDEs) [34–38]. For instance, a pair of coupled Ornstein-Uhlenbeck processes were proposed in [36] to model the coupled evolution of the turn rate and speed of adult zebrafish. Similarly, the jump persistent turning walker was introduced to faithfully capture the burst-and-coast swimming of zebrafish in two [37] and three dimensions [39]. Building on these efforts, mathematical models have addressed the role of spatial

constraints on zebrafish range of vision [40], as well as pharmacological manipulations [41, 42].

Common to this entire body of literature on mathematical modeling of zebrafish locomotion is the premise of a quiescent fluid environment. In its natural habitat, however, zebrafish can experience different flow speeds between 3.5 to 13.9 cm/s [43]. Existing mathematical models exclude the effects of a fluid flow, thereby challenging the study of rheotaxis. To the best of our knowledge, the only mathematical model of fish rheotaxis in the literature is the phenomenological model proposed in [44]. Therein, the authors established a simple model of rheotaxis based on a Kuramoto-like oscillator, which describes fish heading through a bias towards the flow source. Despite its promise, the model does not consider the flow physics nor the multi-sensory feedback that fish should employ to orient and swim in the flow.

A potential line of approach to develop a data-driven model of zebrafish rheotaxis is to leverage recent theoretical results on finite-dipole models of animal swimming [45, 46]. Within the finite-dipole model, a fish is assimilated to a pair of point vortices separated by a finite distance [45], whose strengths can adapt according to behavioral rules [46]. Based on this modeling paradigm, we explore a multi-sensory feedback control system, which allows the animal to adjust its orientation as a function of visual, hydromechanical, and tactile cues.

More specifically, we expand on the finite-dipole paradigm to encompass a data-driven model that allows the fish to adjust the vortex strengths as a function of multi-sensory input from the surroundings. Sensory input from the lateral line, is used to estimate the local circulation of the fluid flow, and visual and tactile cues inform the interaction with the walls. The model is calibrated using a data set consisting of overhead recordings of adult zebrafish swimming in a water channel in standard illumination conditions or in the dark. We demonstrate the effectiveness of our approach by comparing the scoring of behavioral metrics on real and synthetic data from *in-silico* experiments.

Results

Zebrafish swimming as a finite-dipole

We treat a zebrafish as a self-propelled body swimming in two dimensions within a uniaxial inviscid flow, as shown in Figure 1. Here, $(x(t), y(t))$ is the coordinate of the fish centroid in the global reference frame $(\mathcal{X}, \mathcal{Y})$, where t is the time variable. The angle $\theta(t) \in [-\pi, \pi)$ represents the fish heading. For $\theta = -\pi$ the fish is heading upstream, while for $\theta = 0$ it is heading downstream. Following [45, 46], we assimilate the fish to a finite-dipole, consisting of a pair of point vortices separated by a distance l, corresponding to the fish thickness. These two point vortices of circulation strengths $\Gamma_l(t)$ and $\Gamma_r(t)$ describe the fish self-induced propulsion. The fish thickness is about 5 mm for adult zebrafish, which is much smaller than either dimensions of the water channel, $2x_{\max}$ and $2y_{\max}$.

Hence, the time evolution of the fish position and heading angle can be described by the following set of ODEs:

$$\frac{\mathrm{d}x(t)}{\mathrm{d}t} = \frac{\Gamma_l(t) + \Gamma_r(t)}{4\pi l}\cos(\theta(t)) + U(y(t)), \tag{1a}$$

$$\frac{\mathrm{d}y(t)}{\mathrm{d}t} = \frac{\Gamma_l(t) + \Gamma_r(t)}{4\pi l}\sin(\theta(t)), \tag{1b}$$

$$\frac{\mathrm{d}\theta(t)}{\mathrm{d}t} = -U'(y(t))\cos^2(\theta(t)) + \frac{\Gamma_l(t) - \Gamma_r(t)}{2\pi l^2}, \tag{1c}$$

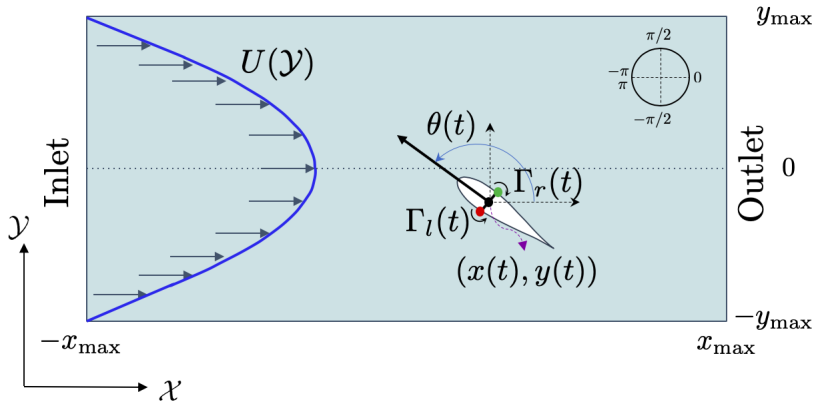

(a)

Fig 1. Modeling zebrafish swimming in a flow as a finite-dipole. $U(\mathcal{Y})$ is the profile of the uniaxial background flow. The black dot and arrow denote the fish centroid position $(x(t), y(t))$ and heading angle $\theta(t)$, with respect to the global reference frame $(\mathcal{X}, \mathcal{Y})$. The green and red dots represent the left and right location of the vortices of circulation strengths $\Gamma_l(t)$ and $\Gamma_r(t)$, respectively.

where $U(\mathcal{Y})$ and $U'(\mathcal{Y})$ are the axial flow velocity and its gradient along the width of the channel, respectively; see Materials and methods for details on the derivation. These scalar spatial fields entirely capture the effect of the background flow on the fish motion.

The vortex strengths encapsulate the self-propelling mechanism along with the feedback contributions for controlling both heading and speed. In particular, $\Gamma_l(t) > \Gamma_r(t)$ indicates that the fish performs a counterclockwise turn, while the opposite, $\Gamma_r(t) > \Gamma_l(t)$, refers to clockwise turns. For $\Gamma_l(t) = \Gamma_r(t)$, the fish swims straight. The fish relative speed with respect to the background flow is $(\Gamma_l(t) + \Gamma_r(t))/(4\pi l)$.

Vortex strengths from experimental data

We conducted an experiment using 24 adult zebrafish swimming in the flow. In order to understand the role of vision on the fish swimming mechanism, we considered two experimental conditions on groups of 12 individuals: Bright and Dark. In Bright, fish swam with standard illumination (250 lx), and in Dark they swam in the darkness. Using an automatic tracking software, we obtained time series for the position of the centroid and the heading angle. These time series were used in equations (1a) and (1b) to estimate the vortex strengths Γ_r and Γ_l for all trials, as described in Materials and methods.

Figures 2(a) and 2(b) exemplify two typical distributions for the vortex strengths of adult zebrafish swimming in a flow for Bright and Dark, respectively. In both cases, the distributions of Γ_l and Γ_r are highly correlated with R^2 values of 0.879 and 0.880, for Bright and Dark, respectively. This suggests that these processes are not independent. In particular, the phase plots in Figures 2(c) and 2(d) indicate that both processes unfold around the line $\Gamma_l = \Gamma_r$ (red dashed-line in Figures 2(c) and 2(d)) with random fluctuations corresponding to turning maneuvers.

The phase plots for the vortex strengths share similarities with phase plots of diffusively coupled dynamical systems, often studied in the context of synchronization [47–49]. Just like oscillators tend to synchronize their phase against noise [50], the two vortices seek to match their circulation strengths against random

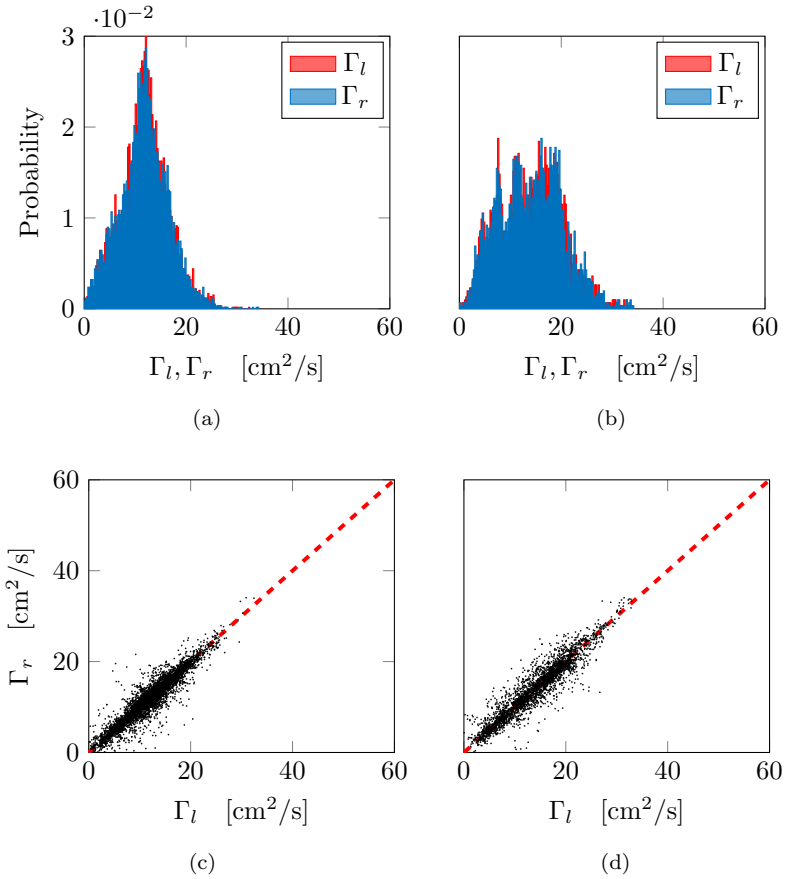

Fig 2. Estimated vortex strengths Γ_l and Γ_r from real data. (a,b) Histograms and (c,d) phase plots of vortex strengths for conditions (a,c) Bright and (b,d) Dark.

fluctuations. Based on this analogy, we hypothesize that the coupling between the processes associated with the circulation strengths is diffusive.

Modeling the time evolution of the vortex strengths

From Figures 2(a) and 2(b), we note that the vortex strengths $\Gamma_l(t)$ and $\Gamma_r(t)$ can be approximated by a Gamma distribution [51]. Based on the analogy with diffusively coupled systems, we propose the following pair of coupled Cox–Ingersoll–Ross processes [52] to model the time evolution of the vortex strengths:

$$\mathrm{d}\Gamma_l(t) = (\alpha(\beta - \Gamma_l(t)) + u(t))\,\mathrm{d}t + \sigma\sqrt{\Gamma_l(t)}\mathrm{d}W_l(t), \tag{2a}$$

$$\mathrm{d}\Gamma_r(t) = (\alpha(\beta - \Gamma_r(t)) - u(t))\,\mathrm{d}t + \sigma\sqrt{\Gamma_r(t)}\mathrm{d}W_r(t), \tag{2b}$$

where α [1/s] and β [cm^2/s] are positive parameters representing the linear rate of decay and a baseline value of the vortex strengths, respectively. The parameter β is associated with the speed of the fish relative to the background flow, whereby $\beta/(2\pi l)$ would be the relative speed of the finite-dipole during straight swimming, without the effect of noise. The positive parameter σ [cm/s] measures the strength of both added noises $W_l(t)$ and $W_r(t)$, which are assumed to be independent Wiener processes [s$^{1/2}$]. $u(t)$ is a feedback term [cm^2/s^2] modeling the coupling between the circulation strengths, the hydromechanical orientation mechanism, and the visual interaction of the

fish with the walls, such that

$$u(t) = \kappa(\Gamma_r(t) - \Gamma_l(t)) + u_{\mathrm{h}}(t) + u_{\mathrm{w}}(t), \tag{3}$$

The feedback term $u(t)$ acts differentially on $\Gamma_l(t)$ and $\Gamma_r(t)$, that is, it takes opposite signs in equations (2a) and (2b) to produce adequate turning maneuvers. For instance, when the fish performs clockwise turns, the vortex strengths should satisfy $\Gamma_l > \Gamma_r$. Then, the feedback would tend to increase Γ_l and decrease Γ_r. The first term on the right hand side of equation (3) corresponds to a classic bidirectional diffusive coupling, with $\kappa\,[1/\mathrm{s}]$ being the coupling strength [49, 50]. This positive parameter is associated with the ability of a fish to resume straight swimming after a maneuver. The diffusive coupling forces both processes to evolve along the synchronization manifold $\Gamma_l = \Gamma_r$, similar to the experiments (Figures 2(c) and 2(d)). The terms $u_{\mathrm{h}}(t)$ and $u_{\mathrm{w}}(t)$ capture the hydromechanical orientation mechanism and wall interactions through visual cues, respectively. Tactile interactions with the walls are separately addressed by modifying equations (2a) and (2b) to account for collisions.

Hydromechanical feedback mechanism

Here, we model the feedback process allowing zebrafish to gather information from hydrodynamic cues and use them to orient in the flow, that is, modulating the vortex strengths through the term $u_{\mathrm{h}}(t)$ in equation (3). Similar to zebrafish larvae [25], we propose that adult zebrafish perform rheotaxis on the basis of an estimate of the local vorticity field. We compute the circulation of the background flow around a circle $\mathcal{C}$ with radius r centered at $(x(t), y(t))$, which approximates the fish perimeter (see Figure 3(a)),

$$L_c(t) = \oint_{\mathcal{C}} \mathbf{U}(\mathbf{s})\,\mathrm{d}\mathbf{s} = -\pi r^2 U'(y(t)). \tag{4}$$

Here, $\mathbf{U}(\mathbf{s}) = [U(s_y), 0]$ is the vector-field of the uni-axial background flow and the last equality is true up to the order $\mathcal{O}(r^4)$; see Materials and methods for details on the derivation. We set $r = 1/2\,\mathrm{BL}$, with $\mathrm{BL} = 3.6\,\mathrm{cm}$ being the average fish body length.

Positive values of $L_c(t)$ indicate that the background flow induces counterclockwise rotations, while negative values refer to induced clockwise rotations. The value of the local circulation $L_c(t)$ depends on the fish position in the swimming channel, as sketched in Figure 3(a). To illustrate how a zebrafish use this information to adjust its heading angle towards the flow, we extracted sixty seconds from the time series of a subject in Bright. In Figure 3(b), we plot the turn rate $\omega(t) = \mathrm{d}\theta(t)/\mathrm{d}t$ and the circulation $L_c(t)$, each normalized between -1 and 1. We further computed the phases of both signals, namely, $\psi_\omega(t)$ and $\psi_{L_c}(t)$ using a Hilbert transform in Matlab (R2019b). We note that zebrafish tend to track (or follow) the rotation induced by the flow (see supplementary video S1 Video). For completeness, in Figure 3(c), we plot $L_c(t)$ against the turn rate $\omega(t)$, which suggests a linear correlation between the variables, such that the fish tendency to turn clockwise or counterclockwise depends on the local circulation of the background flow.

We propose that a fish linearly adjusts its heading on the basis of the local circulation of the flow. First, we verified the tendency of a fish to follow the rotation induced by the background flow. We focused on instances when fish were sufficiently far from the wall such that they could not touch it (1BL away form the walls). We computed the quantity F_c as the percent of the experimental time in which fish turn according to the rotation induced by the background flow. With reference to Figure 3(c), we scored the fraction of points in the first and third quadrants out of the total number of points. We further scored F_c by smoothing the turn rate via a robust

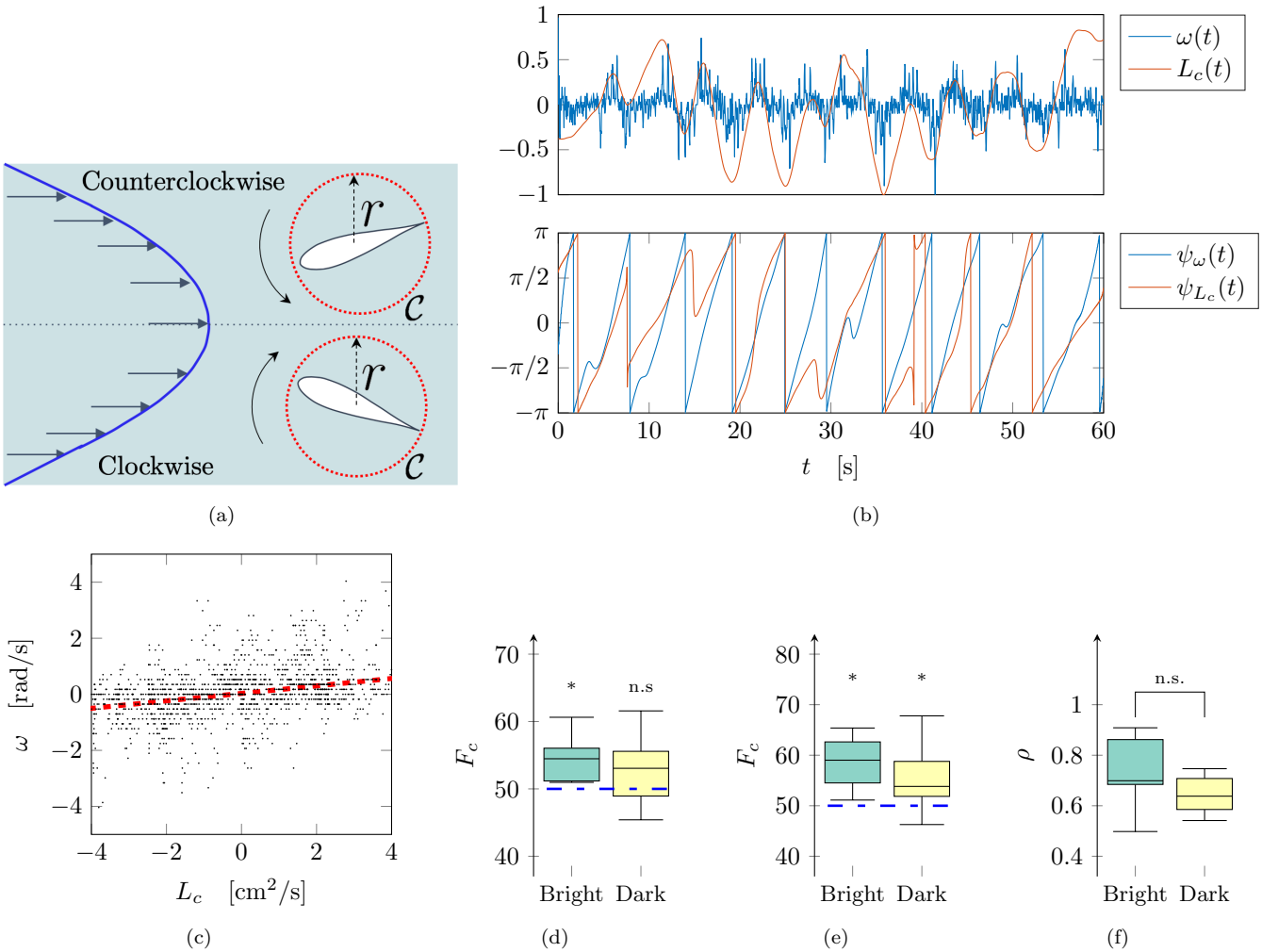

Fig 3. Ability of zebrafish to track the local circulation of the fluid flow. (a) Example of rotation induced by a parabolic flow; the red circle of radius r is the approximation used for the fish perimeter in the computation of the local circulation of the background flow. (b) Time series of the normalized turn rate and normalized local circulation (top panel) and their respective phases (bottom panel), normalized between -1 and 1. (c) Relationship between the rotation induced by the flow (circulation $L_c(t)$) and the turn rate ($\omega(t) = \mathrm{d}\theta(t)/\mathrm{d}t$). The red dashed-line is a linear least-squares fit, on the initial 60 s of the time series, with a slope of 0.163 and $R^2 = 0.151$. Quantification of the ability of a fish to follow local rotations induced by the background flow with and without visual cues using the (d) original or (e) smoothed turn rate. The blue dashed-line represents the random chance level of 50%. Each box reports median, first and third quartiles, and minimum and maximum. Symbol $*$ indicates a significant difference from chance with $p < 0.050$. (f) Synchronization index between the phases of the normalized turn rate and local circulation.

weighted linear least squares in Matlab 2019, to account for oscillations that rapidly change the sign of turns. Finally, we quantified the ability of a zebrafish to track (or follow) the local circulation by scoring the synchronization index [53] $\rho = (1/2)(e^{i\psi_\omega} + e^{i\psi_{L_c}})$ with $i = \sqrt{-1}$, between the phase of the turn rate $\psi_\omega(t)$ and the phase of the circulation $\psi_{L_c}(t)$. A value of $\rho = 0$ indicates the absence of synchronization, while $\rho = 1$ identifies perfect synchronization.

Results of this analysis are shown in Figures 3(d), 3(e), and 3(f). We report a significant difference between chance and the tendency of the fish to follow the rotation

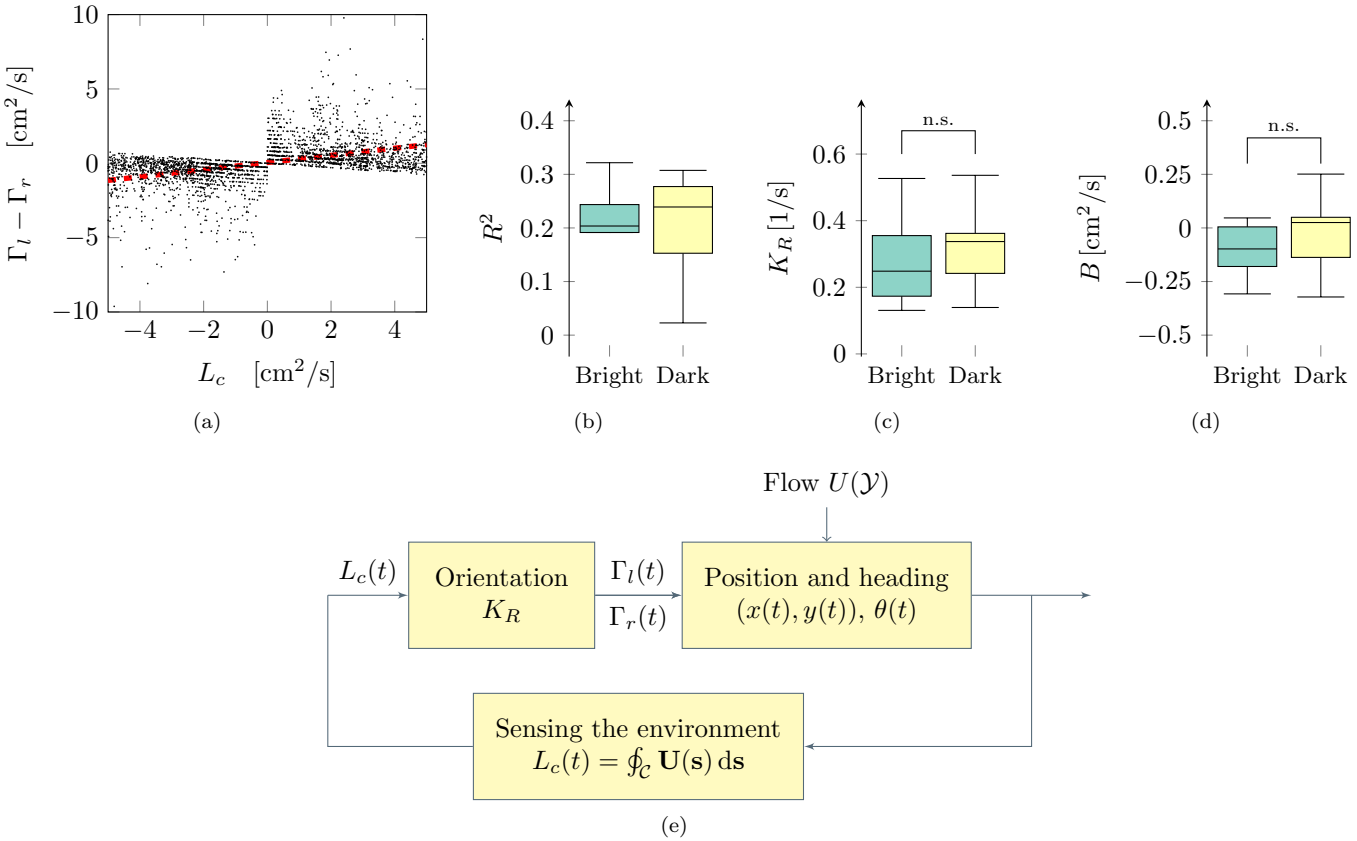

Fig 4. Hydromechanical feedback mechanism in adult zebrafish. (a) Relationship between the local circulation L_c and the difference of vortex strengths $(\Gamma_l - \Gamma_r)$ for instances when the turn rate and local circulation have the same signs, based on the same time series considered in Figure 3(c). The red dashed-line is a linear least-squares fit with slope $K_R = 0.248$ and $R^2 = 0.191$. (b) Goodness-of-fit of the linear relationship between L_c and $\Gamma_l - \Gamma_r$. (c) Analysis of the estimated slope for conditions Bright and Dark. (d) Intercept of the linear regression. Each box reports median, first and third quartiles, and minimum and maximum. (e) Block diagram describing the feedback mechanism to orient in the flow and perform rheotaxis.

of the local curl for condition Bright ($V = 67; p < 0.050$), while for condition Dark we failed to detect a significant difference ($V = 62; p = 0.077$). Using the smoothed turn rate we register a significant difference for both condition Bright ($V = 70; p < 0.050$) and Dark ($V = 65; p < 0.050$). Finally, we did not register a significant difference between condition Bright and Dark ($W = 106; p = 0.053$) with respect to the synchronization index ρ.

Next, we focus on the instances when the turn rate and the circulation match their signs. We investigate the response of the difference of vortex strengths $\Gamma_l(t) - \Gamma_r(t)$ as a function of the circulation $L_c(t)$ as illustrated in Figure 4(a). We fitted a linear model $\Gamma_l - \Gamma_r \sim L_c$ to calculate the goodness-of-fit measure R^2, slope K_R [1/s], and intercept B [cm^2/s] for all trials in both conditions, Bright and Dark. The results are shown in Figures 4(b), 4(c), and 4(d). The regression analysis indicates that a linear model could be used as a first approximation to capture the dependence between the difference in the vortex strengths and the circulation of the background flow. Pairwise comparison between conditions Bright and Dark on the slope K_R and the intercept B did not reveal significant differences (K_R: $W = 59; p = 0.477$ and B: $W = 53; p = 0.291$).

Based on this empirical evidence, we propose that the hydromechanical feedback u_{h} in equation (3) should be a linear function of the local circulation of the background

flow,

$$u_{\mathrm{h}}(t) = K_R L_c(t), \tag{5}$$

where K_R [1/s] is a positive parameter weighting the hydrodynamic information, as illustrated in Figure 4(e). For positive L_c, the fish feedback control mechanism would induce counterclockwise turns as the circulations would satisfy $\Gamma_l > \Gamma_r$, while for negative values of L_c the turns would be clockwise and the vortex strengths satisfy $\Gamma_r > \Gamma_l$.

Wall interaction: visual and tactile feedback

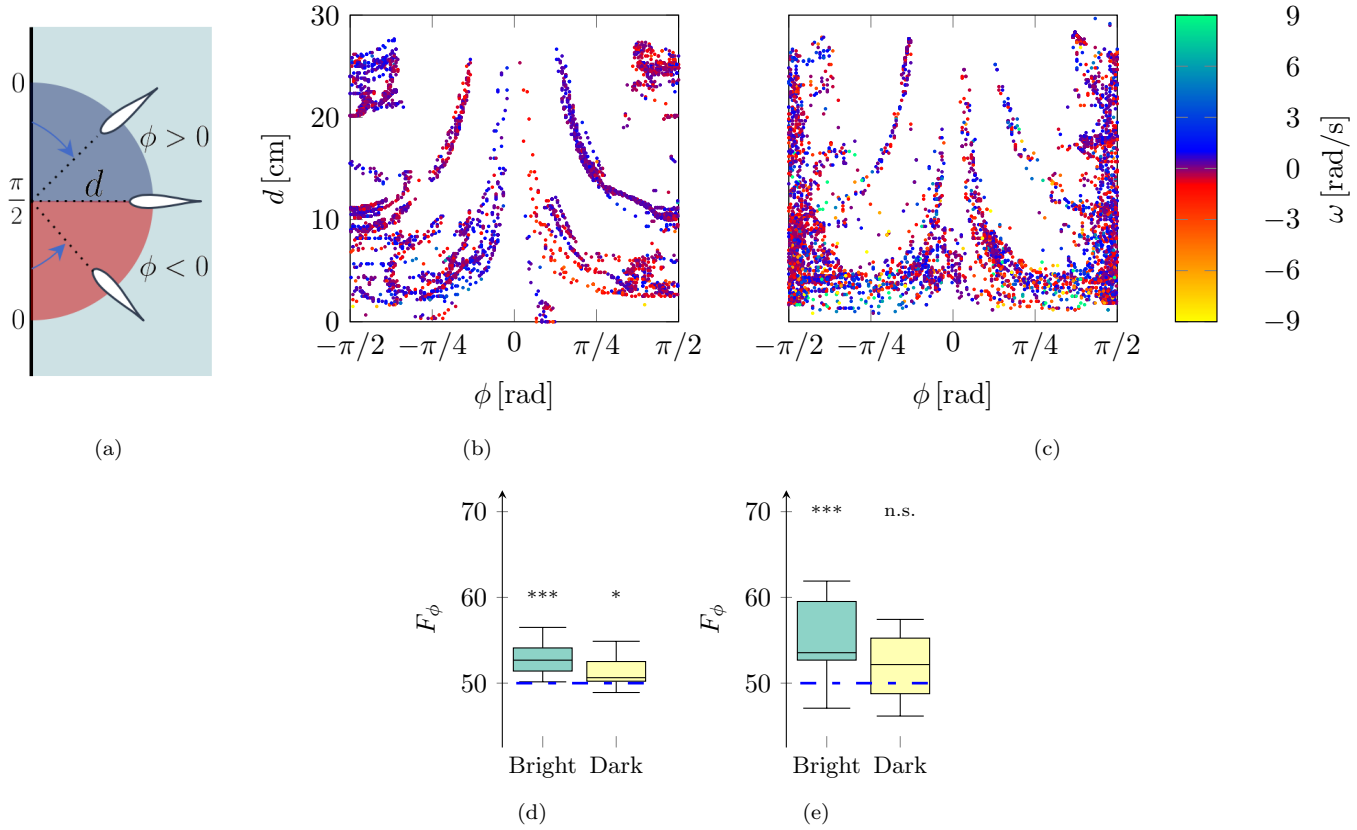

Fig 5. Analysis of the wall interaction. (a) Illustration of the process to compute the projected distance and angle to collision. (b)-(c) Two-dimensional projection of the circulation error as a function of the projected distance, d, and angle to collision, ϕ, for conditions Bright and Dark, respectively. The blue and red color scales denote positive or negative turn rate ω, corresponding to counterclockwise and clockwise turns, respectively. (d) Quantification of the fish ability to turn away from a wall using information about the angle to collision. The blue dashed-line represents the random chance level of 50%. (e) Quantification of fish ability to turn away from a wall for distances to collision less than 1 BL. Each box reports median, first and third quartiles, and minimum and maximum. Symbols $*$ and $***$ indicate a significant difference from chance with $p < 0.050$ and $p < 0.001$, respectively.

Here, we study the interaction of the fish with the walls, which comprises two different feedback mechanisms using vision and touch. Visual feedback is captured through u_{w} in equation (3). Tactile feedback instead is modelled as a collision that modifies the evolution of the vortex strengths with respect to equations (2a) and (2b), as the fish collides with the walls.

Following [34, 36], we quantified the wall effect by measuring the projected distance d and angle of collision ϕ, as illustrated in Figure 5(a). We only considered those instances when the centroid was within 1 BL range from the wall. The angle ϕ is measured from the wall axis to the projected heading vector, as indicated by the blue arrows in Figure 5(a). Specifically, $\phi = \pi/2$ if the fish is heading straight to the wall, and $\phi = 0$ if it is perfectly aligned to the wall axis. In addition, $\phi > 0$ (clockwise) and $\phi < 0$ (counterclockwise) indicate instances when a fish approaches the wall with its right or left side, respectively.

To understand how a fish turns in the vicinity of a wall, we focused on one individual from Bright and one individual from Dark. We plotted the difference in the turn rate $\omega(t)$ as a function of the distance and of the angle to collision, as shown in Figures 5(b) and 5(c). Predictably, the animal swimming in normal lighting conditions tends to turn according to the sign of the angle to collision ϕ. More specifically, the fish preferred to turn clockwise as it approached the wall from its left side, while it tended to rotate counterclockwise if it approached the wall from its right side. The subject swimming in the dark did not exhibit this response, since visual cues were not available for correcting its heading as it swam towards the wall.

From these two representative subjects, we moved forward to the systematic quantification of zebrafish tendency to make turns based on the angle ϕ. Toward this aim, we scored F_ϕ as the percent of instances when the sign of turn rate $\omega(t)$ was the opposite of the sign of ϕ, irrespective of the distance from it. Results are shown in Figure 5(d), where we compared the value of F_ϕ for conditions Bright and Dark with chance. We registered a significant difference for both conditions Bright ($V = 78; p < 0.001$) and Dark ($V = 60; p < 0.050$).

To further delve into how fish interacts with the wall, we examined only instances when they were in close proximity or in direct contact to a wall. In these instances, the animal could exploit other sensing mechanisms beyond vision to avoid the wall. We scored F_ϕ by only considering those instances when the distance to collision d was less than 1 BL. Results are shown in Figure 5(e), where we document a significant difference for condition Bright ($V = 75; p < 0.001$). Although we failed to register a significant difference for Dark ($V = 64; p = 0.052$), this observation offers partial support in favor of the presence of other mechanisms to detect walls when swimming in close proximity.

Following [35], we model the visual feedback as a function of the projected distance and angle of collision which is given by

$$u_{\mathrm{w}}(t) = \frac{K_W}{Cd(t) + 1}\mathrm{sign}(\phi(t)), \tag{6}$$

where K_W [$\mathrm{cm}^2/\mathrm{s}^2$] and C [1/cm] are positive constant parameters capturing the maximum intensity of turns and the decay of the wall effect as a function of the distance d [cm]. In the dark, we assume that animals do not have visual cues and this term is not present in the model, that is, $K_W = 0$.

Next, we model the tactile component of turning in the vicinity of a wall, which is crucial for describing the wall interaction of the fish in the dark. In the vicinity of a wall, turns are captured through

$$\frac{\mathrm{d}\Gamma_l(t)}{\mathrm{d}t} = \eta\,\mathrm{sign}(\phi^-(t)), \qquad \text{for all} \quad |x(t)| > x_{\max} - \epsilon, \quad |y(t)| > y_{\max} - \epsilon, \tag{7a}$$

$$\frac{\mathrm{d}\Gamma_r(t)}{\mathrm{d}t} = -\eta\,\mathrm{sign}(\phi^-(t)), \qquad \text{for all} \quad |x(t)| > x_{\max} - \epsilon, \quad |y(t)| > y_{\max} - \epsilon, \tag{7b}$$

where $\phi^-(t)$ denotes the angle of collision previous to the impact, η [$\mathrm{cm}^2/\mathrm{s}^2$] is the rate of turning once a collision occurs, and ϵ [cm] is an arbitrary small constant representing

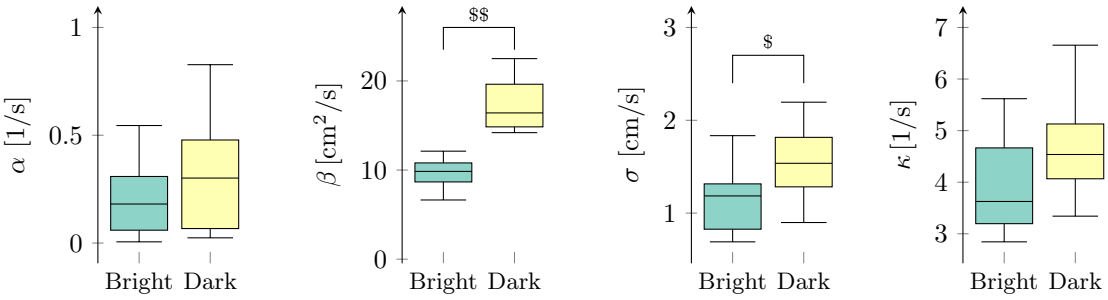

Fig 6. Comparison between calibrated model parameters for conditions Bright and Dark. (a) Linear rate of decay of the vortex strengths. (b) Baseline value of the vortex strengths. (c) Intensity of the noise added to the time-evolution of vortex strengths. (d) Coupling gain between vortex strengths associated with the ability of a fish to resume straight swimming after a maneuver. Each box reports median, first and third quartiles, and minimum and maximum. Symbols $ and $$ indicate significant differences between conditions with $p < 0.050$ and $p < 0.010$, respectively.

wall touching. We heuristically found that setting $\eta = 10\,\mathrm{cm}^2/\mathrm{s}^2$ and $\epsilon = 0.001\,\mathrm{cm}$ reproduces realistic turns, as observed in real experiments.

There is an additional consideration to make for the right wall which corresponds to the test section outlet, shown in Figure 1. In this case, the fish experiences suction forces and could hit the wall while heading in a direction opposite to it, thereby preventing the use of equations (7a) and (7b) for capturing the impact. To account for this case and counter-balance the suction force, we should modify equations (7a) and (7b) as follows:

$$\frac{\mathrm{d}\Gamma_l(t)}{\mathrm{d}t} = \eta, \qquad \text{for all} \quad x(t) > x_{\max} - \epsilon, \quad |\theta(t)| > \frac{\pi}{2}, \tag{8a}$$

$$\frac{\mathrm{d}\Gamma_r(t)}{\mathrm{d}t} = \eta, \qquad \text{for all} \quad x(t) > x_{\max} - \epsilon, \quad |\theta(t)| > \frac{\pi}{2}. \tag{8b}$$

Here, the constraint on the heading angle guarantees that the animal is heading in the opposite direction to the right wall. Also, the signs in equations (8a) and (8b) are both positive, indicating that the interaction with this particular wall is repulsive to counter the suction force.

Model validation: comparison between real and *in-silico* experiments

We calibrated our model using experimental data, as detailed in Material and methods; the resulting parameter values are shown in Figure 6 for both conditions Bright and Dark. We found that the condition significantly influenced the baseline value of the circulation strengths β ($W = 17; p < 0.010$), and the intensity of added noise σ ($W = 37; p < 0.050$). We did not register a significant difference on the linear rate of decay of the vortex strengths α ($W = 64; p = 0.670$) and the coupling strength κ ($W = 37; p = 0.079$). Supplementary videos S2 Video and S3 Video show exemplary instances of rheoactic behavior predicted by the mathematical model in conditions Bright and Dark, respectively.

In order to validate the predictive power of our model, we compared the scoring of two different metrics used to quantify rheotaxis, the mean of (negative) cosine of the heading and the mean rheotaxis index (RI); see Materials and methods for a mathematical definition. Both metrics take values between -1 and 1 corresponding to biased headings towards downstream and upstream, respectively. A zero value represents the case in which a fish does not have a preference to swim either upstream or downstream.

From the results in Figure 7, in the real experiments, we determined that the cosine of the heading was different from chance in both Bright ($V = 78; p < 0.001$) and Dark ($V = 71; p < 0.010$). Likewise, for the RI we registered significant differences from chance in both Bright ($V = 78; p < 0.001$) and Dark ($V = 68; p = 0.021$). In pairwise comparisons between Bright and Dark, we identified a superior rheotactic response for animals swimming in standard illumination conditions, with respect to the cosine of the heading ($W = 134; p < 0.001$) and RI ($W = 134; p < 0.001$). Finally, to measure locomotory activity of the animal in the form of exploration of the entire test section, we calculated the spatial entropy; see Materials and methods for a mathematical definition. The comparison between the two conditions suggest the presence of a trend, with fish swimming in the dark displaying a higher locomotory activity than subjects swimming in standard illumination conditions ($W = 40; p = 0.068$). This trend was accompanied by a significant difference of the variance of the spatial entropy between conditions, ($F = 12.053; p < 0.010$), with animals swimming in the dark displaying a lower variability.

Equivalent relationships were predicted by *in-silico* experiments. In these experiments, we used a five times larger sample size to improve statistical power. Two outliers were detected using the iterquantile range rule [54] on the spatial entropy variable and thus neglected from the analysis. The cosine of the heading differed from chance in both Bright ($V = 1711; p < 0.001$) and Dark ($V = 1711; p < 0.001$). Similarly, RI registered significant differences in both Bright ($V = 1711; p < 0.001$) and Dark ($V = 1711; p < 0.001$). Pairwise comparisons between Bright and Dark indicated significant differences for the cosine of the heading ($W = 2944; p < 0.001$), RI ($W = 2947; p < 0.001$), spatial entropy ($W = 854; p < 0.001$), and variance of spatial entropy ($F = 4.279; p < 0.050$).

Discussion

Rheotaxis is a complex multi-sensory process that involves the integration of different cues to orient in a flow and engage in counter-flow swimming. Toward a better understanding of how fish interacts with their surroundings and integrate different sensory cues during rheotaxis, we developed a data-driven mathematical model of zebrafish swimming in a flow. With respect to the state of knowledge on data-driven modeling of zebrafish locomotion, this study contributes the first mathematical model of swimming in a fluid flow. To generalize existing data-driven models that were intentionally developed for studying swimming in quiescient fluids [34–38], we tap into recent advancements in hydrodynamic modeling of fish swimming based on the finite-dipole paradigm [45, 46].

The proposed modeling framework is articulated in three main steps: (i) multi-sensing, through which the fish appraises its surroundings from visual, hydrodynamic, and tactile cues; (ii) orientation and navigation control, which uses the multi-sensory input to modulate the vortex strengths that are associated with self-propulsion; and (iii) motion in the flow based on the finite-dipole model, as a function of the background flow and the circulation strengths of the vortex pair.

Our results indicate that hydromechanical cues play a key role on the orientation and navigation whereby the fish tends to make turns by following the rotation induced by the flow, regardless of the availability of visual cues. This suggests that information about the environment provided by the lateral line alone is sufficient to perform rheotaxis. This is also evident in our calibrated model parameters, where the feedback gain that is associated with hydromechanical sensory information did not vary with the illumination conditions. Our findings are in line with previous results in the literature, where it has been shown that the lateral line organ is fundamental to aid the orientation

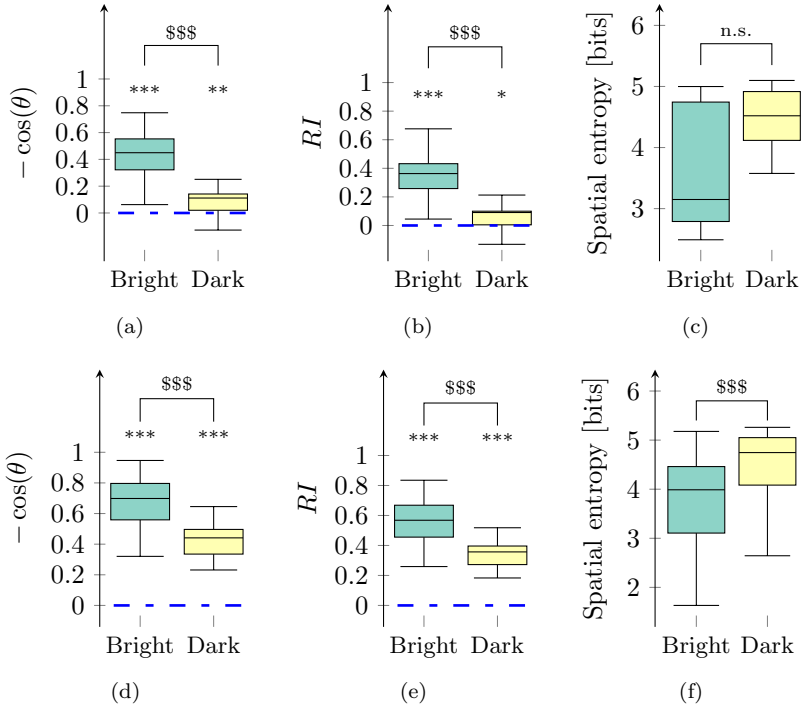

Fig 7. Scoring of three behavioral metrics for real and *in-silico* experiments. Rheotactic metrics taking values between -1 and 1 corresponding to biased headings towards downstream and upstream, respectively, for real (a,b) and synthetic (d,e) data. Spatial entropy for real (c) and synthetic (f) data. Each box reports median, first and third quartiles, and minimum and maximum. Symbols $*$, $**$ and $***$ indicate significant differences from zero with $p < 0.050$, $p < 0.010$, and $p < 0.001$, respectively. Symbol \$\$\$ indicates significant difference between conditions with $p < 0.001$.

process of fish [20, 24].

In a uniaxial flow, the feedback mechanism used by zebrafish reduces to tracking the gradient of the background flow. Specifically, the difference in the vortex strengths of the finite-dipole model is linearly controlled by the variation of the axial flow with respect to the width of the test section. Orientation strategies based on gradients have also been observed in other biological domains such as light gradient sensing in fish [55] where animals are able to track variations of light intensity and adjust their maneuvers [56]. Another example is chemical gradient sensing in cells [57, 58], where chemoattractant fields are sensed by proteins whose information is then used to modulate the orientation of the cell.

We observed that the scoring of behavioral metrics in real experiments was successfully paralleled by simulations. In particular, fish swimming in the dark displayed a higher locomotory activity in the test section, when compared to subjects in standard illumination conditions. Increased activity is likely related to an anxiety-related response, which is triggered by the presence of a dark, threatening environment, as widely documented in zebrafish literature on scototaxis [59]. *In-silico* experiments are also successful in predicting a significantly lower rheotactic performance for animals swimming in the dark. While sensing local circulation through the lateral line is not affected by the presence of visual cues, animal locomotion varies with the illumination conditions. Specifically, the mathematical model identifies that animals swimming in the dark have a higher relative speed with respect to the background flow

than subjects in standard illumination conditions. This increased speed challenges the ability of zebrafish to adjust their orientation in response to the gradient of the background flow during rheotaxis.

Our approach has limitations that call for future research. First and foremost, the data-driven mathematical model focuses on two-dimensional swimming, thereby preventing the possibility of studying diving maneuvers along the height of the test section. Several studies [60–62] have pointed out the critical role of diving maneuvers on the response of this freshwater species, thereby suggesting the use of a three-dimensional ethogram for scoring zebrafish behavior. Three-dimensional effects are also likely to play a role on the difference between the rheotaxis metrics of real and *in-silico* experiments, whereby live animals have access to a richer flow physics than the two-dimensional background flow used in the simulations. Extending the proposed approach to three dimensions poses a number of methodological challenges, which requires a more complex representation than a vortex pair to encapsulate zebrafish swimming. Second, we cannot exclude that zebrafish might exploit other systems for performing rheotaxis, such as the vestibular system [26, 27]. Disentangling the contribution of the vestibular system would require further experimental conditions, potentially involving the selective impairment of the potentially contributing sensory systems.

In summary, we proposed a simple, yet effective, multi-sensory feedback control process for describing rheotaxis of an adult zebrafish. In particular, we incorporated three types of sensory feedback mechanism relying on visual, hydromechanical, and tactile cues. Interestingly, our model suggests that the gradient of the flow profile is the key information that drives rheotactic behavior. Similar to zebrafish larvae [25], our model indicate that rheotacting adults tend to follow the negative direction of the velocity gradient to adjust their orientation and swim upstream.

Materials and methods

Ethics statement

Experiments were performed in accordance with the guidelines and regulations approved by the University Animal Welfare Commitee (UAWC) of New York University under protocol number 13-1424.

Animal care and maintenance

A total of 24 wild-type adult zebrafish (*Danio rerio*), 12 male and 12 female, were used in this study. The fish were purchased from Carolina Biological Supply Co. (Burlington, NC, USA), and housed in a 615 L vivarium tank divided into two compartments to mantain sexes separated. Fish were kept under a 12 h light/12 h dark photo-period and fed with commercial flake food once a day, approximately at 7 PM. Water parameters of the holding tanks were regularly checked, and temperature and pH were maintained at 26°C and 7.2, respectively. Prior to the beginning of the experiments, fish were acclimatized in the holding facility for one month.

Experimental apparatus

The experimental set-up (Figure 8(a)) consisted of a 151 L Blazka-type water channel (Engineering Laboratory Design Inc., Lake City, MI, USA), a video camera (Logitech C910 HD Pro Webcam without infrared filter, Logitech, Switzerland) located at the bottom of the channel, an array of lights, and black curtains to minimize outside visual stimuli. We used two different lighting systems for the Bright and Dark conditions. In

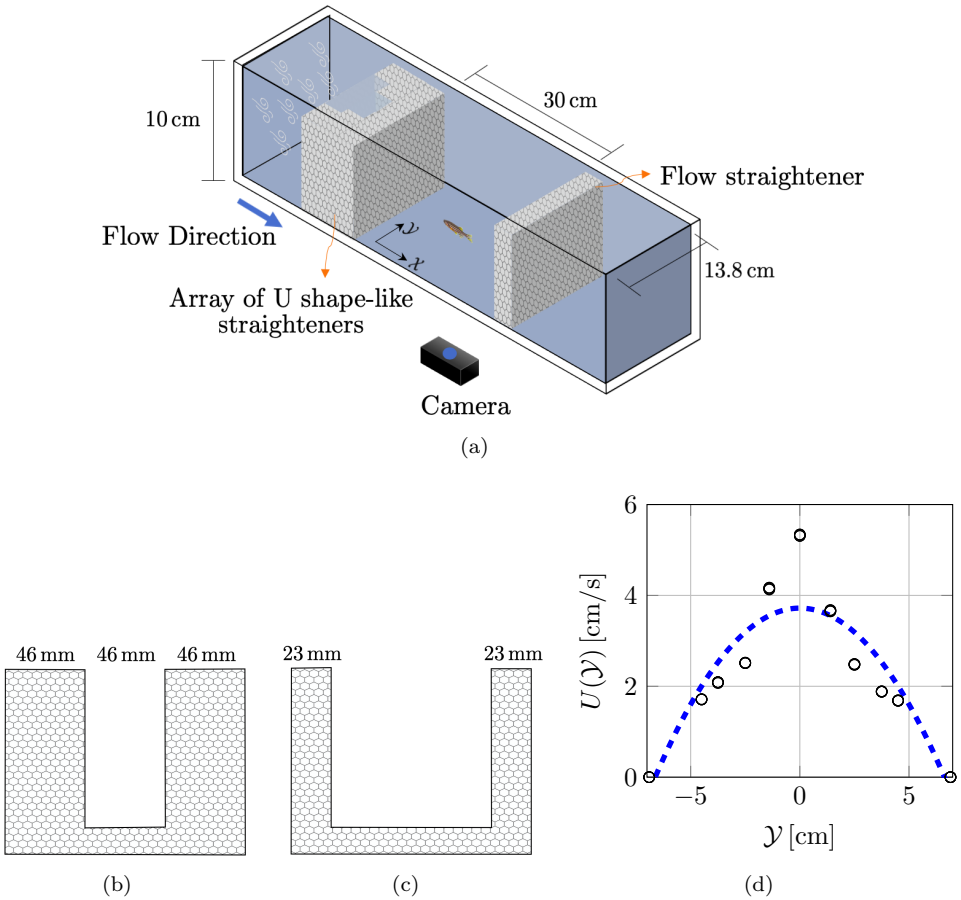

Fig 8. Experimental set-up. (a) Overview of the experimental apparatus. (b,c) U shape-like honeycomb grids for straightening the flow in the water channel. (d) Measurements of the flow velocity profile and parabolic fit at the mid-span.

particular, for the Bright condition, we used a pair of fluorescent lamps (Aqueon Full Spectrum Daylight T8, Aqueon, USA) located at the top of the channel along with a white plexiglass sheet to dim the light intensity and provide a homogeneous light background of 250 lx. For recording fish swimming in the dark, we used infrared lights (Iluminar IRC99 Series, Iluminar, Irvine, CA) with wavelength 940 nm, which is greater than the adult zebrafish threshold of spectral sensitivity [63]. Two pairs of infrared lights were located at the bottom and top of the water channel to provide a clear background for recording videos in the dark.

A test section of 30 cm × 13 cm ($2x_{\max} \times 2y_{\max}$) at a water height of 10 cm was arranged within the channel using flow straighteners, as shown in Figure 8(a). The flow profile was created using an array of U-shaped flow straighteners with different opening sizes to manipulate the flow speed (Figures 8(b) and 8(c)). The flow velocity was measured at the mid-span of the test section using a Laser Doppler Velocimeter (BSA F50, Dantec, Denmark). We obtained five velocity measurements for nine different points across the test section ($\mathcal{Y}$-coordinate). The flow velocity measurements along with the fitted parabolic flow profile is shown in Figure 8(d). The maximum speed was 5.3 cm/s, which was on the order of 1 BL/s. The fitting was performed using standard least squares in Matlab (R2019b) yielding $U(\mathcal{Y}) = -0.084\mathcal{Y}^2 + 3.720$, with the velocity measured in cm/s and position in cm.

Experimental procedure

Two different illumination conditions were tested, namely Bright and Dark. Each trial consisted of three main phases. The first two phases were introduced for habituation to the new environment and the flow, while the third phase was the actual testing. Only the last phase was recorded. At the beginning of the trial, the animal was transferred from the vivarium to the water tunnel (using a hand net) and kept there for five minutes of habituation with the water velocity set to zero. Then, the water flow was turn on for two minutes of further habituation and five minutes of testing. A total of 24 naïve adult fish were tested, 12 (6 male and 6 female) for each condition (Bright and Dark).

Tracking

A total of 300 s were recorded for each trial at 30 frames per second. All videos were post-processed using a foreground detection algorithm in Matlab (R2019b) for highlighting the animal shape on the image and improve the tracking process [64]. The resulting images were input to a slightly modified version of the multi-target tracking algorithm Peregrine [65], accounting for manual repairs in body shape tracking mode. The software fitted a parabola on the fish blob and returned: the fish centroid position $(x(t), y(t))$ with their respective velocities, shape parameters (coefficients of the parabola), and heading vector $\mathbf{h} = [\cos(\theta(t)), \sin(\theta(t))]$, from which the heading angle and turn rate were calculated.

Statistical analyses and behavioral scoring

All statistical analyses were performed with the statistics software R (version 3.6.1). We used the Wilcoxon signed-rank test and the Mann-Whitney U test (Wilcoxon rank sum), with a significance level of 0.050, for comparing one-sample and two-sample data, respectively [66]. For testing the equality of two-sample data variances we use the Levene's test [67] with a significance level of 0.050.

To study rheotaxis, we averaged the time series of $-\cos(\theta(t))$ in each trial, and we scored RI, defined as the difference between the cumulative distribution functions of the absolute value of the heading and a uniform random variable [27]. More specifically, $RI = 1 - (2/\pi)\int_0^\pi \Lambda(|\theta|)\,\mathrm{d}\theta$, with $\Lambda(\cdot)$ being the empirical cumulative distribution function. Here, $\pi/2$ represents the area under the curve of an empirical cumulative distribution function of a uniform random variable over the interval $[0, \pi]$.

We further quantified the fish exploratory behavior in the test section through spatial entropy. This quantity was measured by first dividing the test section in 10×4 squares of approximately $3\,\mathrm{cm} \times 3.25\,\mathrm{cm}$ each, corresponding to a grid of 1 BL in size. Then, using the centroid trajectory $(x(t), y(t))$, we estimated the probability of occupying each boxes in the grid, p_i. The spatial entropy is then given by $-\sum_{i=1}^{40} p_i \log_2(p_i)$.

In-silico experiments

We replicated the real experiment by considering 24 trials, 12 for Bright and 12 for Dark. We numerically integrated equations (1), (2), (3), (5), and (6) using the Euler-Maruyama scheme with a time step of $1/30\,\mathrm{s}$, matching the sampling rate of the tracked data). To ensure convergence to a steady state probability distribution, we chose a simulation time of six times the experimental time (6×300 s), and we only considered the last 300 s. The parameter values α, κ, and K_R were taken from Gaussian distributions corresponding to the data across all 24 trials (Bright and Dark). Because the parameters β and σ were significantly different between Bright and Dark, their values were drawn from two different Gaussian distributions for each parameter,

corresponding to the data shown in Figure 6(b) and Figure 6(c), respectively. Given that the test section is rectangular, unrealistic turns or oscillations might arise on the corners due to their discontinuous nature [36]. To avoid this problem, we kept the angle to collision constant when the fish was inside a square region of $1\,\mathrm{cm}^2$ on the corners.

Derivation of the governing equations of the finite-dipole model

The zebrafish dipole representation is depicted in Figure 1. By adapting the equation set (2) from [46], the centroid position and heading angle can be obtained by integrating the following set of ODEs:

$$\frac{\mathrm{d}x(t)}{\mathrm{d}t} = \frac{\Gamma_l(t)+\Gamma_r(t)}{4\pi l}\cos(\theta(t)) + \frac{U(y_r(t))+U(y_l(t))}{2}, \tag{9a}$$

$$\frac{\mathrm{d}y(t)}{\mathrm{d}t} = \frac{\Gamma_l(t)+\Gamma_r(t)}{4\pi l}\sin(\theta(t)), \tag{9b}$$

$$\frac{\mathrm{d}\theta(t)}{\mathrm{d}t} = \frac{U(y_r(t))-U(y_l(t))}{l}\cos(\theta(t)) + \frac{\Gamma_l(t)-\Gamma_r(t)}{2\pi l^2}, \tag{9c}$$

where

$$y_l(t) = y(t) + \frac{l}{2}\cos(\theta(t)), \quad y_r(t) = y(t) - \frac{l}{2}\cos(\theta(t)). \tag{10}$$

Considering that the animal thickness, $l \sim 5$ mm, is small with respect to the dimensions of the water channel, we expand the velocity field at the location of the two vortices, $U(y_r(t))$ and $U(y_l(t))$, around the centroid coordinate $y(t)$ using a Taylor series, yielding

$$U(y_l(t)) = U(y(t)) + U'(y(t))\frac{l}{2}\cos(\theta(t)) + \frac{U''(y(t))}{2}\left(\frac{l}{2}\cos(\theta(t))\right)^2 + \frac{U'''(y(t))}{6}\left(\frac{l}{2}\cos(\theta(t))\right)^3 + \mathcal{O}(l^4), \tag{11a}$$

$$U(y_r(t)) = U(y(t)) - U'(y(t))\frac{l}{2}\cos(\theta(t)) + \frac{U''(y(t))}{2}\left(\frac{l}{2}\cos(\theta(t))\right)^2 - \frac{U'''(y(t))}{6}\left(\frac{l}{2}\cos(\theta(t))\right)^3 + \mathcal{O}(l^4), \tag{11b}$$

where $\mathcal{O}(\cdot)$ is Landau's symbol. By considering a first order approximation in equations (11a) and (11b), we determine

$$\frac{U(y_r(t))+U(y_l(t))}{2} \simeq U(y(t)), \tag{12a}$$

$$\frac{U(y_r(t))-U(y_l(t))}{l} \simeq -U'(y(t))\cos(\theta(t)). \tag{12b}$$

Finally, replacing equations (12a) and (12b) in equations (9a)-(9c) yields equations (1a)-(1c).

Estimation of the circulation strengths from experimental time series

To estimate the circulation strengths we used experimental data of the fish centroid position $(x(t), y(t))$, heading angle $\theta(t)$, and turn rate $\omega(t)$. Using a first order

approximation, equations (9a)-(9c) can be written as

$$\widetilde{x}(kT) = \frac{T}{4\pi l}(\Gamma_l(kT) + \Gamma_r(kT))\cos(\theta(kT)), \tag{13a}$$

$$\widetilde{y}(kT) = \frac{T}{4\pi l}(\Gamma_l(kT) + \Gamma_r(kT))\sin(\theta(kT)), \tag{13b}$$

$$\widetilde{\omega}(kT) = \frac{1}{2\pi l^2}(\Gamma_l(kT) - \Gamma_r(kT)). \tag{13c}$$

Here, $k = 1, 2, ..., N-1$ is the time step, $T = 1/30$ s is the video-camera sampling period, $N = 9000$ is the total number of samples, and

$$\widetilde{x}(kT) = x((k+1)T) - x(kT) - \frac{(U(y_r(kT)) + U(y_l(kT)))T}{2}, \tag{14a}$$

$$\widetilde{y}(kT) = y((k+1)T) - y(kT), \tag{14b}$$

$$\widetilde{\omega}(kT) = \omega(kT) - \frac{U(y_r(kT)) - U(y_l(kT))}{l}\cos(\theta(kT)), \tag{14c}$$

with $U(y_r(kT))$ and $U(y_l(kT))$ being the flow velocities in correspondence of the right $y_r(kT) = y(kT) - (l/2)\cos(\theta(kT))$ and left $y_l(kT) = y(kT) + (l/2)\cos(\theta(kT))$ vortices, respectively.

By squaring both sides of equations (13a) and (13b), we determine that

$$\sqrt{\widetilde{x}^2(kT) + \widetilde{y}^2(kT)} = \frac{T}{4\pi l}(\Gamma_l(kT) + \Gamma_r(kT)), \tag{15}$$

Finally, from equations (13c) and (15) we obtain the sought expression of the circulations strengths as function of fish motion

$$\Gamma_l(kT) = \pi l\left(\frac{2}{T}\sqrt{\widetilde{x}^2(kT) + \widetilde{y}^2(kT)} + l\widetilde{\omega}(kT)\right), \tag{16a}$$

$$\Gamma_r(kT) = \pi l\left(\frac{2}{T}\sqrt{\widetilde{x}^2(kT) + \widetilde{y}^2(kT)} - l\widetilde{\omega}(kT)\right). \tag{16b}$$

Expansion of the line integral for the local circulation

The fish perimeter is approximated by a circle $\mathcal{C}$ around the fish centroid $(x(t), y(t))$ defined by

$$s_x = x(t) + r\cos(\varphi), \quad s_y = y(t) + r\sin(\varphi), \quad \text{for all } \varphi \in [0, 2\pi]. \tag{17}$$

The line integral in equation (4) is thus given by

$$\oint_{\mathcal{C}} \mathbf{U}(\mathbf{s})\,\mathrm{d}\mathbf{s} = -r\int_0^{2\pi} U(y(t) + r\sin(\varphi))\sin(\varphi)\,\mathrm{d}\varphi. \tag{18}$$

By a using a Taylor expansion of the velocity around $y(t)$, we establish

$$\begin{aligned}\oint_{\mathcal{C}} \mathbf{U}(\mathbf{s})\,\mathrm{d}\mathbf{s} = &-r\int_0^{2\pi} U(y(t))\sin(\varphi)\,\mathrm{d}\varphi - r^2\int_0^{2\pi} U'(y(t))\sin^2(\varphi)\,\mathrm{d}\varphi \\ &- \frac{r^3}{2}\int_0^{2\pi} U''(y(t))\sin^3(\varphi)\,\mathrm{d}\varphi + \mathcal{O}(r^4).\end{aligned} \tag{19}$$

Finally, from the fact that $\int_0^{2\pi}\sin(\varphi)\,d\varphi = 0$, $\int_0^{2\pi}\sin^2(\varphi)\,d\varphi = \pi$, and $\int_0^{2\pi}\sin^3(\varphi)\,d\varphi = 0$ we derive equation (4).

Model calibration

We began by approximating the solutions of the stochastic differential equations in equation (2a) and (2b) away from the wall (neglecting u_{h} and u_{w}) and with no u_{h}, using the Euler-Maruyama method, thereby yielding the following Markov chain:

$$\begin{aligned}\Gamma_l((k+1)T) &= \Gamma_l(kT) + \left[\alpha(\beta - \Gamma_l(kT)) + \kappa(\Gamma_r(kT) - \Gamma_l(kT))\right]T \\ &\quad + \sigma\sqrt{\Gamma_l(kT)T}\,\xi_l(kT), \qquad (20a)\\ \Gamma_r((k+1)T) &= \Gamma_r(kT) + \left[\alpha(\beta - \Gamma_r(kT)) + \kappa(\Gamma_l(kT) - \Gamma_r(kT))\right]T \\ &\quad + \sigma\sqrt{\Gamma_r(kT)T}\,\xi_r(kT), \qquad (20b)\end{aligned}$$

where ξ_l and ξ_r are two independent standard Gaussian random variables, with zero mean and unit variance. After some algebraic manipulations, equations (20a) and (20b) can be rewritten as

$$Z_l(kT) := f(\Gamma_l(kT), \Gamma_l((k+1)T), \Gamma_r(kT), \alpha, \beta, \sigma, \kappa) = \sqrt{\left(\frac{\sigma}{K_0}\right)^2 T}\,\xi_l(kT), \qquad (21)$$

$$Z_r(kT) := f(\Gamma_r(kT), \Gamma_r((k+1)T), \Gamma_l(kT), \alpha, \beta, \sigma, \kappa) = \sqrt{\left(\frac{\sigma}{K_0}\right)^2 T}\,\xi_r(kT), \qquad (22)$$

where the scalar function $f(X, Y, Z, \alpha, \beta, \sigma, \kappa)$ is given by

$$f(X, Y, Z, \alpha, \beta, \sigma, \kappa) = \frac{Y + X(\alpha T + \kappa T - 1) - \alpha\beta T - \kappa T Z}{K_0\sqrt{X}}, \qquad (23)$$

with K_0 being an arbitrary positive constant, introduced to avoid numerical issues when the circulations strengths are close to zero. To calibrate the model we estimated the parameters $\mathbf{\Theta} = [\alpha, \beta, \sigma/K_0, \kappa]$ using the maximum likelihood estimation method [68] by solving the following constrained optimization problem:

$$\widehat{\mathbf{\Theta}} = \arg\min_{\mathbf{\Theta}} \left[-\sum_{k=1}^{N^*} \log g(\mathbf{\Theta}, Z_l(kT)) + \log g(\mathbf{\Theta}, Z_r(kT))\right] \qquad (24a)$$

$$\text{such that} \quad \sigma^2 < 2\alpha\beta, \qquad (24b)$$

where $N^* < N$ is the total number of samples where the fish was swimming away from the wall. The function $g(\mathbf{\Theta}, Z)$ is the Gaussian distribution with zero mean and variance $(\sigma/K_0)^2 T$, given by

$$g(\mathbf{\Theta}, Z) = \frac{1}{\sqrt{2\pi T\left(\frac{\sigma}{K_0}\right)^2}}\, \mathrm{e}^{-\frac{Z^2}{2T\left(\frac{\sigma}{K_0}\right)^2}}. \qquad (25)$$

The estimated parameters are shown in Table 1 for the 24 experimental trials.

Moreover, for calibrating the wall parameters in equation (6), we implemented the following steps:

(i) We first extracted instances when the fish turns according to the opposite sign of the angle to collision ϕ, that is, blue points ($\Gamma_l - \Gamma_r > 0$) for $\phi < 0$ and red points ($\Gamma_l - \Gamma_r < 0$) for $\phi > 0$ as shown in Figure 9(a). To undertake this step, we utilized a cutoff function, which was informed by the following rationale. As the angle ϕ approaches $\pm\pi/2$ or the distance to collision d increases, fish turns becomes less predictable. Hence, we retained pairs (ϕ, d) such that $|g(\phi) - d| < \delta$

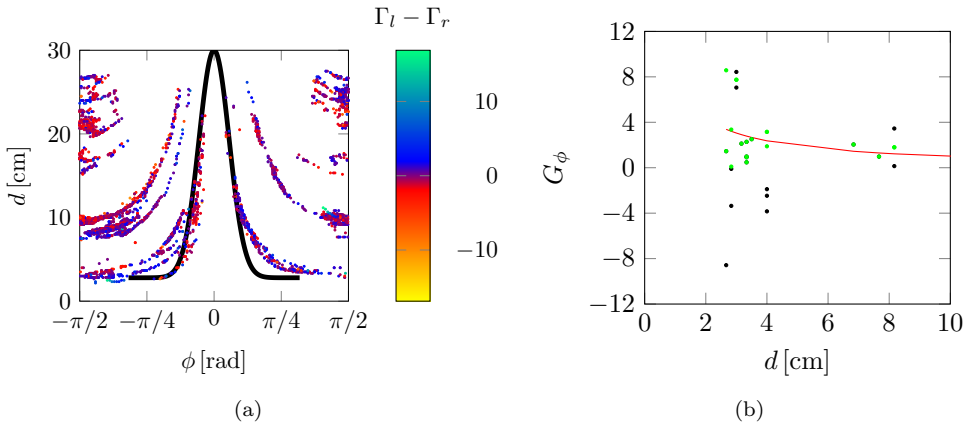

Fig 9. Illustration of the wall calibration process. (a) Two-dimensional projection of the difference of vortex strengths $\Gamma_l - \Gamma_r$, as a function of the projected distance, d, and angle to collision, ϕ, for one trial from Bright. The black curve is a normal function utilized to select relevant values of (ϕ, d) associated with those instances when the fish turns according to the angle to collision ϕ. (b) Example of calibration of the wall function. Black dots correspond to G_ϕ and green dots correspond to the filtered output of $|G_\phi|$. The red line is the fitted wall function.

Table 1. Calibrated model parameters for the 24 experimental trials.

	Bright					Dark				
	Parameters									
Trial	α[1/s]	β[cm^2/s]	σ[cm/s]	κ [1/s]	K_R [1/s]	α[1/s]	β[cm^2/s]	σ[cm/s]	κ [1/s]	K_R [1/s]
1	0.030	10.602	0.808	3.536	0.173	0.082	21.870	1.282	4.740	0.241
2	0.306	10.223	1.185	3.655	0.248	0.024	-	1.328	4.066	0.358
3	1.020	18.348	3.078	-	0.490	0.750	11.944	0.898	6.452	0.056
4	0.059	6.6422	0.889	5.411	0.190	0.246	16.410	1.653	3.919	0.316
5	0.005	-	0.826	3.842	0.526	0.049	26.949	0.927	6.656	0.139
6	0.545	10.638	1.475	3.397	0.245	0.495	15.737	2.061	4.537	0.536
7	0.177	8.1365	0.690	5.618	0.130	0.827	22.502	2.194	4.472	0.337
8	0.308	9.4714	1.193	3.597	0.355	0.402	14.197	1.711	4.347	0.409
9	0.235	9.197	1.314	2.843	0.278	0.301	15.494	1.536	5.283	0.361
10	0.754	12.118	1.834	4.733	0.310	0.477	17.387	1.816	5.128	0.328
11	0.153	10.960	1.133	4.597	0.170	0.472	16.858	1.362	3.341	0.338
12	0.181	9.2510	1.281	2.995	0.428	0.067	-	1.884	4.947	0.381

and $|\phi| < \phi_0$, where ϕ_0 and δ are cutoff parameters and $g(\phi) = a_g + b_g\, e^{-(\phi/c_g)^2}$ (Black curve in 9(a)). By manually examining the 12 trials in Bright, we found that setting $\phi_0 = 1$, $a_g = 2.8$, $b_g = 27.2$, $c_g = 0.26$, and $\delta = 1$ was a valid choice to extract all relevant maneuvers.

(ii) To understand how fish turn based on the vicinity to a wall, we defined G_ϕ as the quantity collecting the values of the difference of circulation strengths $(\Gamma_l - \Gamma_r)$, corresponding to the points (ϕ, d) obtained from the previous step. For the example shown in Figure 9(a), the points G_ϕ correspond to black dots. Next, we used a non-parametric locally weighted least squares (LOESS) filter in Matlab (R2019b) with a 5% span on the absolute value of G_ϕ to smoothen the data. The results are the green dots shown in Figure 9(b);

(iii) The output of the LOESS filter, y_d, was utilized as input to fit the wall function

$K_W/(Cy_d + 1)$ using the nonlinear least-squares solver of Matlab (R2019b). The fitted function corresponds to the red curve in Figure 9(b) and

(iv) Because we used the difference of circulation strengths for the fitting, the estimate of K_W should be corrected to obtain the true amplitude of turns corresponding to each circulation strengths. Hence, we computed the maximum value of Γ_l and Γ_r across all time instances near a wall. K_W was selected as the maximum between the values obtained in (iii) and (iv). Results are reported in Table 2.

Table 2. Calibrated wall parameters for the 12 fish tested in standard illumination (condition Bright). For experiments in the dark, K_W is set to zero and this form of interaction is absent.

Trial	K_W [1/s]	C [cm]
1	23.085	-
2	52.905	2.072
3	70.379	2.775
4	29.168	-
5	34.114	1.853
6	86.376	2.119
7	20.251	-
8	37.540	2.674
9	34.721	2.351
10	37.858	2.210
11	38.686	-
12	45.593	3.078
Mean	42.556	2.392
Median	37.699	2.281

Supporting information

S1 Video. Experiment of a subject in Bright condition: tracking the local circulation of the fluid flow.

S2 Video. Example of rheotaxis predicted by the proposed mathematical model in condition Bright.

S3 Video. Example of rheotaxis predicted by the proposed mathematical model in condition Dark.

S4 Dataset.

Acknowledgment

We wish to thank Jeremy Kupuprika for his help in building an initial version of the experimental set-up. We also thank Dr. Peng Zhang for his constructive discussions on fluid dynamics and Dr. Ghania Benbelkacem for her help with the final experimental set-up and animal tracking. Further, we would like to thank all members of the Dynamical System Laboratory for valuable comments on a first version of the

manuscript. This work was supported by the National Science Foundation under grants CMMI-1505832 and CMMI-1901697.

Author contributions

MP supervised the research and secured the funding. DB and MP conceived and designed the study. DB performed the experiments, wrote the computer codes, and performed the analysis. DB wrote a first draft of the paper, which MP consolidated into the present submission.

Data Availability

All relevant data are within the manuscript and its Supporting Information file S4 Dataset.

References

1. Able KP. Orientation and navigation: a perspective on fifty years of research. The Condor. 1995;97(2):592–604.
2. Gould JL, Gould CG. Nature's compass: the mystery of animal navigation. vol. 16. Princeton University Press; 2012.
3. Dressler F, Akan OB. A survey on bio-inspired networking. Computer Networks. 2010;54(6):881–900.
4. Flamarique IN, Browman HI. Foraging and prey-search behaviour of small juvenile rainbow trout (*Oncorhynchus mykiss*) under polarized light. Journal of Experimental Biology. 2001;204(14):2415–2422.
5. Namiki S, Kanzaki R. The neurobiological basis of orientation in insects: insights from the silkmoth mating dance. Current Opinion in Insect Science. 2016;15:16–26.
6. Wang Z, Schaefer HM. Resting orientation enhances prey survival on strongly structured background. Ecological Research. 2012;27(1):107–113.
7. Del Valle M. Bioinspired Sensor Systems. Sensors. 2011;11(11):10180.
8. Werfel J, Petersen K, Nagpal R. Designing collective behavior in a termite-inspired robot construction team. Science. 2014;343(6172):754–758.
9. Putman NF, Lohmann KJ, Putman EM, Quinn TP, Klimley AP, Noakes DL. Evidence for geomagnetic imprinting as a homing mechanism in Pacific salmon. Current Biology. 2013;23(4):312–316.
10. Hasler AD, Scholz AT. Olfactory imprinting and homing in salmon: Investigations into the mechanism of the imprinting process. vol. 14. Springer Science & Business Media; 2012.
11. Mafra-Neto A, Cardé RT. Fine-scale structure of pheromone plumes modulates upwind orientation of flying moths. Nature. 1994;369(6476):142–144.

12. Chapman JW, Klaassen RH, Drake VA, Fossette S, Hays GC, Metcalfe JD, et al. Animal orientation strategies for movement in flows. Current Biology. 2011;21(20):R861–R870.

13. Toma DP, White KP, Hirsch J, Greenspan RJ. Identification of genes involved in *Drosophila melanogaster* geotaxis, a complex behavioral trait. Nature Genetics. 2002;31(4):349–353.

14. Sawin EP, Harris LR, Campos AR, Sokolowski MB. Sensorimotor transformation from light reception to phototactic behavior in Drosophila larvae (*Diptera: Drosophilidae*). Journal of Insect Behavior. 1994;7(4):553.

15. Olszewski J, Haehnel M, Taguchi M, Liao JC. Zebrafish larvae exhibit rheotaxis and can escape a continuous suction source using their lateral line. PLoS ONE. 2012;7(5).

16. Montgomery J, Coombs S, Halstead M. Biology of the mechanosensory lateral line in fishes. Reviews in Fish Biology and Fisheries. 1995;5(4):399–416.

17. Montgomery JC, Baker CF, Carton AG. The lateral line can mediate rheotaxis in fish. Nature. 1997;389(6654):960–963.

18. Elder J, Coombs S. The influence of turbulence on the sensory basis of rheotaxis. Journal of Comparative Physiology A. 2015;201(7):667–680.

19. Arnold G. The reactions of the plaice (*Pleuronectes platessa L.*) to water currents. Journal of Experimental Biology. 1969;51(3):681–697.

20. Suli A, Watson GM, Rubel EW, Raible DW. Rheotaxis in larval zebrafish is mediated by lateral line mechanosensory hair cells. PLoS One. 2012;7(2).

21. Hassan ES. Hydrodynamic imaging of the surroundings by the lateral line of the blind cave fish *Anoptichthys jordani*. In: The mechanosensory lateral line. Springer; 1989. p. 217–227.

22. Bleckmann H, Zelick R. Lateral line system of fish. Integrative Zoology. 2009;4(1):13–25.

23. Windsor SP, Norris SE, Cameron SM, Mallinson GD, Montgomery JC. The flow fields involved in hydrodynamic imaging by blind Mexican cave fish (*Astyanax fasciatus*). Part II: gliding parallel to a wall. Journal of Experimental Biology. 2010;213(22):3832–3842.

24. Baker C, Montgomery J. The sensory basis of rheotaxis in the blind Mexican cave fish, *Astyanax fasciatus*. Journal of Comparative Physiology A. 1999;184(5):519–527.

25. Oteiza P, Odstrcil I, Lauder G, Portugues R, Engert F. A novel mechanism for mechanosensory-based rheotaxis in larval zebrafish. Nature. 2017;547(7664):445–448.

26. Olive R, Wolf S, Dubreuil A, Bormuth V, Debrégeas G, Candelier R. Rheotaxis of larval zebrafish: behavioral study of a multi-sensory process. Frontiers in Systems Neuroscience. 2016;10:14.

27. Bak-Coleman J, Paley DA, Coombs S, et al. The spatiotemporal dynamics of rheotactic behavior depends on flow speed and available sensory information. Journal of Experimental Biology. 2013;216(21):4011–4024.

28. Nusslein-Volhard C, Dahm R. Zebrafish. Oxford University Press; 2002.

29. Gerlai R. Fish in behavior research: unique tools with a great promise! Journal of Neuroscience Methods. 2014;234:54–58.

30. Cassar S, Adatto I, Freeman JL, Gamse JT, Iturria In, Lawrence C, et al. Use of zebrafish in drug discovery toxicology. Chemical Research in Toxicology. 2019;33(1):95–118.

31. Kalueff AV, Stewart AM, Gerlai R. Zebrafish as an emerging model for studying complex brain disorders. Trends in Pharmacological Sciences. 2014;35(2):63–75.

32. Friedrich R, Genoud C, Wanner AA. Analyzing the structure and function of neuronal circuits in zebrafish. Frontiers in Neural Circuits. 2013;7:71.

33. McHenry MJ, Lauder GV. The mechanical scaling of coasting in zebrafish (*Danio rerio*). Journal of Experimental Biology. 2005;208(12):2289–2301.

34. Gautrais J, Jost C, Soria M, Campo A, Motsch S, Fournier R, et al. Analyzing fish movement as a persistent turning walker. Journal of Mathematical Biology. 2009;58(3):429–445.

35. Gautrais J, Ginelli F, Fournier R, Blanco S, Soria M, Chaté H, et al. Deciphering interactions in moving animal groups. PLoS Computational Biology. 2012;8(9).

36. Zienkiewicz A, Barton DA, Porfiri M, Di Bernardo M. Data-driven stochastic modelling of zebrafish locomotion. Journal of Mathematical Biology. 2015;71(5):1081–1105.

37. Mwaffo V, Anderson RP, Butail S, Porfiri M. A jump persistent turning walker to model zebrafish locomotion. Journal of The Royal Society Interface. 2015;12(102):20140884.

38. Calovi DS, Litchinko A, Lecheval V, Lopez U, Escudero AP, Chaté H, et al. Disentangling and modeling interactions in fish with burst-and-coast swimming reveal distinct alignment and attraction behaviors. PLoS Computational Biology. 2018;14(1):e1005933.

39. Mwaffo V, Butail S, Porfiri M. In-silico experiments of zebrafish behaviour: modeling swimming in three dimensions. Scientific Reports. 2017;7(1):1–18.

40. Calovi DS, Lopez U, Schuhmacher P, Chaté H, Sire C, Theraulaz G. Collective response to perturbations in a data-driven fish school model. Journal of The Royal Society Interface. 2015;12(104):20141362.

41. Mwaffo V, Porfiri M. Turning rate dynamics of zebrafish exposed to ethanol. International Journal of Bifurcation and Chaos. 2015;25(07):1540006.

42. Burbano-L DA, Porfiri M. Data-driven modeling of zebrafish behavioral response to acute caffeine administration. Journal of Theoretical Biology. 2020;485:110054.

43. Arunachalam M, Raja M, Vijayakumar C, Malaiammal P, Mayden RL. Natural history of zebrafish (*Danio rerio*) in India. Zebrafish. 2013;10(1):1–14.

44. Chicoli A, Bak-Coleman J, Coombs S, Paley D. Rheotaxis performance increases with group size in a coupled phase model with sensory noise. The European Physical Journal Special Topics. 2015;224(17-18):3233–3244.

45. Tchieu AA, Kanso E, Newton PK. The finite-dipole dynamical system. Proceedings of the Royal Society A: Mathematical, Physical and Engineering Sciences. 2012;468(2146):3006–3026.

46. Gazzola M, Tchieu AA, Alexeev D, de Brauer A, Koumoutsakos P. Learning to school in the presence of hydrodynamic interactions. Journal of Fluid Mechanics. 2016;789:726–749.

47. Pikovsky A, Rosenblum M, Kurths J. Synchronization: A universal concept in nonlinear science; 2003.

48. Tang Y, Qian F, Gao H, Kurths J. Synchronization in complex networks and its application–a survey of recent advances and challenges. Annual Reviews in Control. 2014;38(2):184–198.

49. Pecora LM, Carroll TL. Synchronization of chaotic systems. Chaos: An Interdisciplinary Journal of Nonlinear Science. 2015;25(9):097611.

50. Caraballo Garrido T, Kloeden PE. The persistence of synchronization under environmental noise. Proceedings-Royal Society Mathematical, Physical and Engineering Sciences, 461 (2059), 2257-2267. 2005;.

51. Papoulis A. Random Variables and Stochastic Processes. McGraw Hill; 1965.

52. Cox JC, Ingersoll Jr JE, Ross SA. A theory of the term structure of interest rates. In: Theory of Valuation. World Scientific; 2005. p. 129–164.

53. Strogatz SH. From Kuramoto to Crawford: exploring the onset of synchronization in populations of coupled oscillators. Physica D: Nonlinear Phenomena. 2000;143(1-4):1–20.

54. Navidi WC. Statistics for engineers and scientists. McGraw-Hill Higher Education New York, NY, USA; 2008.

55. Puckett JG, Pokhrel AR, Giannini JA. Collective gradient sensing in fish schools. Scientific Reports. 2018;8(1):1–11.

56. Chen X, Engert F. Navigational strategies underlying phototaxis in larval zebrafish. Frontiers in Systems Neuroscience. 2014;8:39.

57. Jin T. Gradient sensing during chemotaxis. Current Opinion in Cell Biology. 2013;25(5):532–537.

58. Onsum M, Rao CV. A mathematical model for neutrophil gradient sensing and polarization. PLoS Computational Biology. 2007;3(3).

59. Maximino C, de Brito TM, da Silva Batista AW, Herculano AM, Morato S, Gouveia Jr A. Measuring anxiety in zebrafish: a critical review. Behavioural Brain Research. 2010;214(2):157–171.

60. Macrì S, Clément RJ, Spinello C, Porfiri M. Comparison between two-and three-dimensional scoring of zebrafish response to psychoactive drugs: identifying when three-dimensional analysis is needed. PeerJ. 2019;7:e7893.

61. Cachat J, Stewart A, Utterback E, Hart P, Gaikwad S, Wong K, et al. Three-dimensional neurophenotyping of adult zebrafish behavior. PLoS ONE. 2011;6(3).

62. Rosa LV, Costa FV, Canzian J, Borba JV, Quadros VA, Rosemberg DB. Three-and bi-dimensional analyses of the shoaling behavior in zebrafish: Influence of modulators of anxiety-like responses. Progress in Neuro-Psychopharmacology and Biological Psychiatry. 2020; p. 109957.

63. Shcherbakov D, Knörzer A, Espenhahn S, Hilbig R, Haas U, Blum M. Sensitivity differences in fish offer near-infrared vision as an adaptable evolutionary trait. PLoS ONE. 2013;8(5).

64. Stauffer C, Grimson WEL. Adaptive background mixture models for real-time tracking. In: Proceedings. 1999 IEEE Computer Society Conference on Computer Vision and Pattern Recognition (Cat. No PR00149). vol. 2. IEEE; 1999. p. 246–252.

65. Bartolini T, Butail S, Porfiri M. Temperature influences sociality and activity of freshwater fish. Environmental Biology of Fishes. 2015;98(3):825–832.

66. Hollander M, Wolfe DA, Chicken E. Nonparametric Statistical Methods. vol. 751. John Wiley & Sons; 2013.

67. Gastwirth JL, Gel YR, Miao W. The impact of Levene's test of equality of variances on statistical theory and practice. Statistical Science. 2009; p. 343–360.

68. Lo AW. Maximum likelihood estimation of generalized Itô processes with discretely sampled data. Econometric Theory. 1988;4(2):231–247.